Supplementary Information (SI)

Increase in anionic Fe_3O_4 nanoparticles-induced membrane poration and vesicle deformation due to membrane potential – an experimental study

Md. Moniruzzaman[1], Mohammad Abu Sayem Karal[1]*, Md. Abdul Wadud[2], and Md. Mamun Or Rashid[2]

[1]Department of Physics, Bangladesh University of Engineering and Technology, Dhaka-1000, Bangladesh
[2]Department of Pharmacy, Noakhali Science and Technology University, Noakhali 3814, Bangladesh

SI 1. Synthesis and concentration of NPs

The magnetite NPs were synthesized using the green synthesis method.[1] The synthesis procedure of NPs is described shortly. At first, *Ipomoea Aquatica* leaf (available in Bangladesh) was bought from the local market, and washed using MilliQ water as shown in Fig. SI 1 (a)(i). The leaf was dried in an oven at 60 °C, and pasted using a blender. An amount of 30 g of paste was mixed with 100 mL of MilliQ water. It was heated at 80 °C and stirred at 800 rpm for 4 h. The leaf extracts were filtered using a filter paper, and collected the solution (Fig. SI 1 (a)(ii)). At first, 10 mL of 0.05 M $FeCl_2{\cdot}4H_2O$ and 10 mL of 0.10 M $FeCl_3$ were stirred at 800 rpm for 10 min keeping the temperature at 60 °C, followed by 5 mL leaf extracts added. After 10 min of mixing, 10 mL of 0.10 M NaOH was added. NPs were precipitated at the bottom of the solution while adding the NaOH. The reaction scheme is as follows,

Ipomoea aquatica + $FeCl_2{\cdot}4H_2O$ (aq) + $2FeCl_3$ (aq) + 8NaOH (aq) → [*Ipomoea aquatica* / Fe_3O_4] ↓(s) + 8NaCl + $8H_2O$ (aq)

The NPs were precipitated at the bottom of a glass beaker, and then collected using a bar magnet. These NPs were dried for a couple of days at 60 °C, and then grinded for fine powder (Fig. SI 1(a)(iii). The size distribution of the synthesized NPs was obtained from dynamic light scattering (DLS) as shown in Fig. SI 1(b). The average size of NPs was 18.0 ± 0.5 nm (here ± indicates SErr). The zeta potential of the synthesized NPs was −21.3 ± 4.8 mV (here ± indicates

SD) (Fig. SI 1(c)), indicating anionic in nature. A series of experiments was conducted using these combinations, and consistent results were obtained. The selection of these values was based on prior evidence and the expected outcomes derived from the synthesis method employed. By considering established knowledge and previous findings, these combinations were determined to be suitable for achieving the desired results in the experiments.

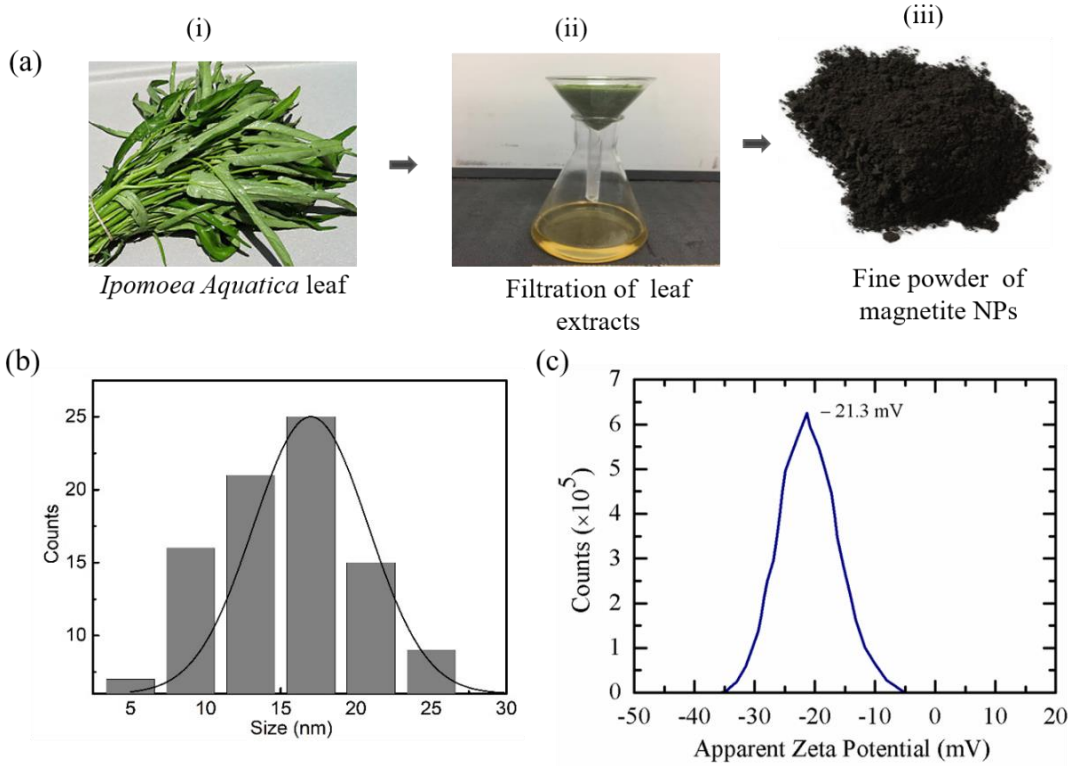

Fig. SI 1 Synthesis and characterization of magnetite NPs. (a) Step wise process for preparing the *Ipomoea aquatica* leaf extracts mediated magnetite NPs. (i) *Ipomea aquatica* leaf, (ii) Leaf extracts, and (iii) Fine powder of NPs. (b) Average size of NPs. (c) Zeta potential of NPs. (b) is reprinted from ref [1] and (c) is reprinted from ref [2] with permission.

The initial solution was prepared by dissolving NPs at 0.025 mg/mL in a mixture consisting of 76% diethylene glycol (DEG) and 24% buffer A. Next, the solution was subjected to sonication for a duration of 30 minutes to ensure proper dissolution of the NPs. The initial solution was diluted in buffer T, resulting in a 0.002 mg/mL NPs solution. This new solution contained 6% DEG, 92% buffer T, and 2% buffer A. Subsequently, 100 µL of the 0.002 mg/mL NPs was mixed with 200 µL of GUVs in buffer T. Then the final concentration of NPs in the microchamber was 0.7 µg/mL in buffer T. The NPs solution contained a negligible percentage of DEG (~ 2%) and buffer A (~ 0.7%). Using a similar approach, NPs solutions of 0.7, 2.0 and 3.3 µg/mL were prepared in buffer T.

SI 2. Observation of GUVs

In order to investigate the effects of membrane potential on the membrane permeation of encapsulating calcein and the deformation of vesicles induced by NPs, we employed the GUVs suspension method.[2,3] In this approach, 200 µL of purified GUVs were appropriately diluted in the microchamber using the corresponding buffer, depending on the desired membrane potential. The microchamber, as shown in Fig. SI 2, comprised a glass slide, a silicon sheet, and a cover slip, forming a U-shaped structure. Subsequently, the microchamber was positioned on the microscope stage, allowing the GUVs to settle for a period of 5-10 minutes. After the settling period, 100 µL of NPs solution was added to the microchamber, resulting in a total volume of 300 µL comprising the GUVs suspension and NPs.

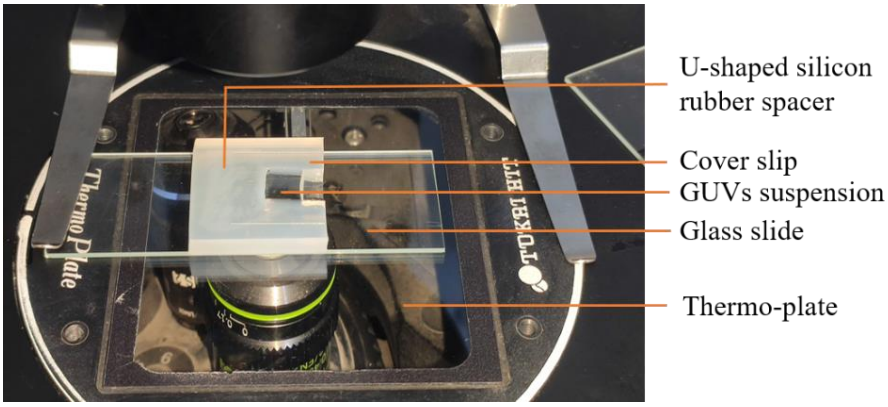

Fig. SI 2 A photo of microchamber used for the observations of GUVs.

SI 3. Generating membrane potential across the lipid bilayer

The membrane potential (φ_m) across the bilayer is generated due to the concentration gradient between the inner and outer regions of the bilayer. Various concentrations of K^+ ion differences were applied for generating different φ_m.[4,5] In this regard, several ratios of purified GUVs and buffer T were transferred into the microchamber. The potential gradient was established by blocking the entrance of GrA of the outer monolayer of the membrane.[6] As the size of TEA^+ is larger than the diameter of GrA, it can easily block the protein channel to stop the exchange of K^+ ions between the inside and outside of the bilayer.[7] An illustration of Fig. SI 3 is provided for generating the φ_m.

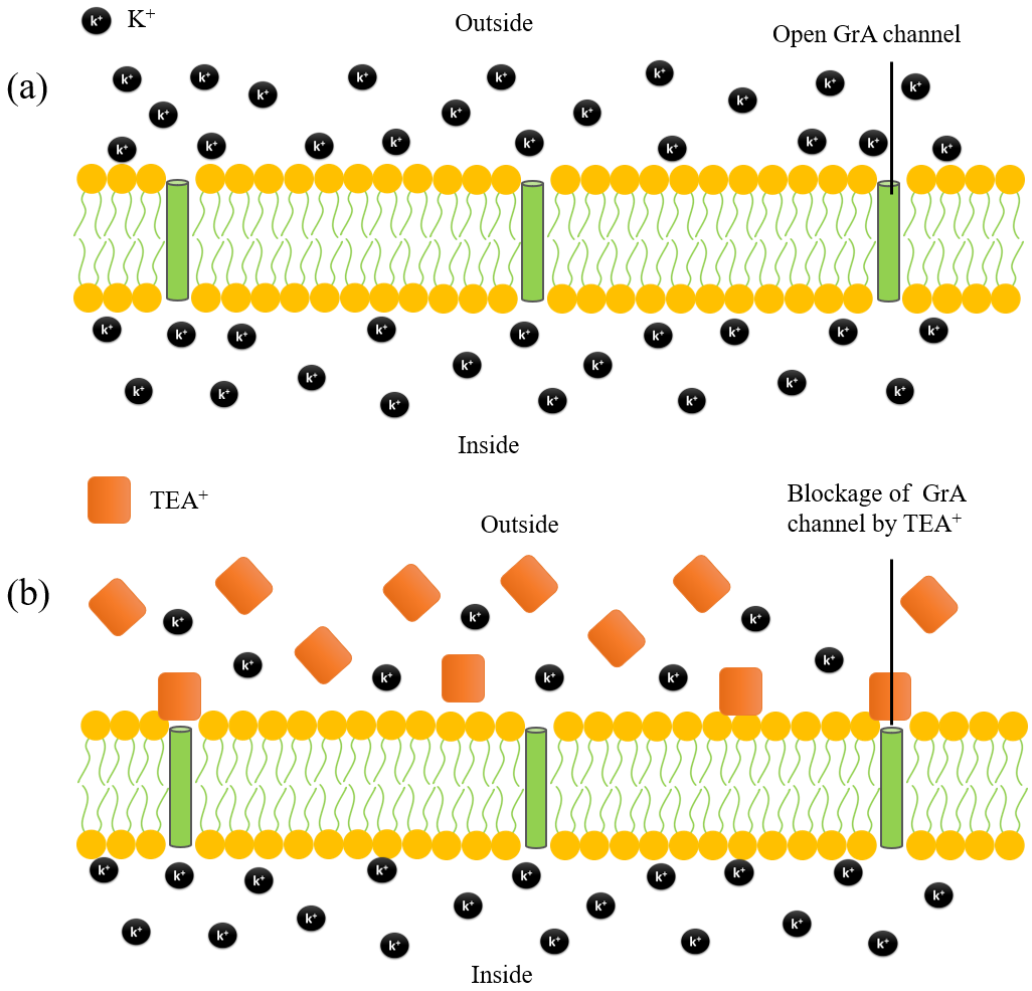

Fig. SI 3 Generating membrane potential across the bilayer due to the concentration gradient of ions between the inside and outside of membrane. (a) At φ_m = 0 where only K^+ ion is used. Here, GrA channels are open, which can transport the K^+ ions, and no concentration gradient is presented. (b) In the presence of φ_m where the channels are blocked by TEA^+ ions and a concentration gradient of K^+ ions are presented.

An example of applying −30 mV membrane potential across the bilayer is described here. The concentration of K^+ ions in buffer B was $[K^+]_{in}$= 150 mM, which was used inside the GUV. The outside K^+ concentration is required $K^+ = 150e^{-25.7/30}$ = 46.6 mM. To obtain a total 200 µL suspension (GUV s and buffer T) in the microchamber, the required amount of GUVs (200 µL × 46.6 mM)/150 mM = 62.1 µL, and buffer T is (200 – 62.2) = 137.9 µL. In the similar way, other φ_m such as −60 and −90 mV were created across the bilayer. We did not quantitatively measure the membrane potential using a membrane potential-sensitive dye, such as DiOC6(3). Instead, we referenced the relevant literature in the main text for the

calculation of the membrane potential. Specifically, the Nernst equation was utilized to estimate the membrane potential in our study.

SI 4. Experiment on DOPG/DOPC/GrA (40/60/0.01)-GUVs without leakage of encapsulating calcein

We conducted a controlled experiment involving the interaction of 2.0 μg/mL NPs with DOPG/DOPC/GrA (40/60/0.01)-GUVs. The experimental results are depicted in Fig. SI 4. Fig. SI 4(a)(i) displays the phase contrast image of a GUV before the addition of NPs at 0 s. Following the introduction of NPs, Fig. SI 4(a)(ii) shows the corresponding fluorescent image of the same GUV. Notably, the encapsulating fluorescence intensity (shown in white) remained constant throughout the entire observation period. At 240 s, Fig. SI 4(a)(iii) presents the phase contrast image of the GUV, demonstrating that the GUV maintained its spherical and intact structure. There were no discernible differences in contrast between the inside and outside of the GUV at both 0 and 240 s. Fig. SI 4(b) illustrates the time-dependent fluorescence intensity of the GUV, as depicted in Fig. SI 4(a). The graph demonstrates that the fluorescence intensity within the GUV lumen remained nearly unchanged throughout the entire observation period.

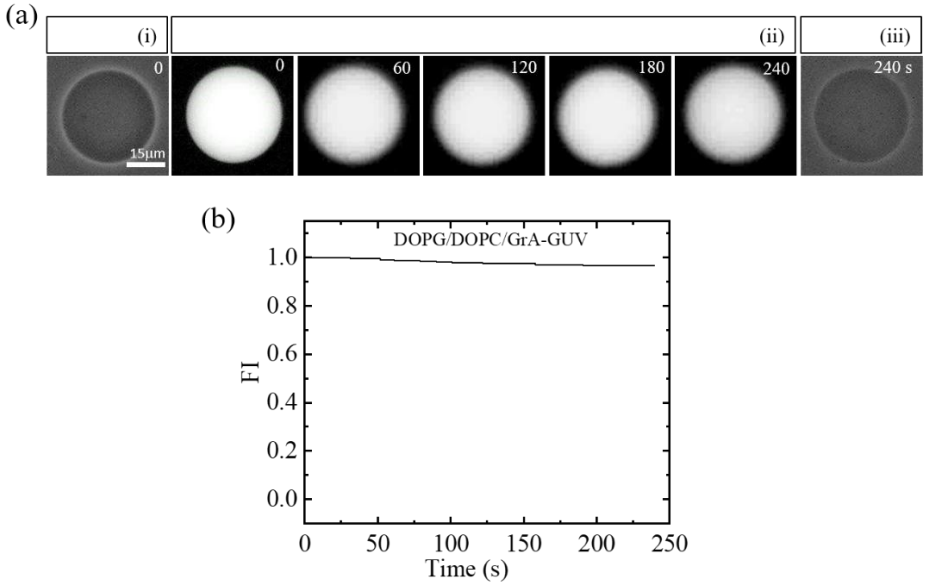

Fig. SI 4 Experiment on DOPG/DOPC/GrA (40/60/0.01)-GUVs without leakage of encapsulating calcein due to the interaction of 2.0 μg/mL NPs. (a) Phase contrast and fluorescent image of a single GUV before application of NPs. (i) and (iii) is the phase contrast images before and after 240s, respectively. (ii) The florescence images of the same GUV. (b) The time course of the change in florescence intensity (FI) of the GUV as shown in (a).

SI 5. NPs-induced encapsulating calcein leakage of DOPG/DOPC/GrA (40/60/0.01)-GUVs at φ_m = −30 and −60 mV

In this section, we describe the calcein leakage of DOPG/DOPC/GrA (40/60/0.01)-GUVs induced by 2.0 µg/mL NPs at φ_m = −30 and −60 mV. The real-time recorded images of 2 'single GUVs' are shown in Fig. SI 5(a) and SI 5(b). The number on the images indicates the time after adding NPs to the suspension of vesicles. The phase contrast image of the GUV before the addition of NPs (i.e., 0 s) is shown in Fig. SI 5((a)(i) and (b)(i)). The fluorescent image of the same GUV after adding NPs is shown in Fig. SI 5((a)(ii) and (b)(ii)). The encapsulating fluorescence intensity (white color) remained the same until a specific time and then decreased slowly. The phase contrast image of the same GUV at 240 s is shown in Fig. SI 5 ((a)(iii) and (b)(iii)), where the rim of the GUV became intact and spherical. Fig. (SI 5(c) and (e)) is the corresponding time-dependent fluorescence intensity of the GUV represented in Fig. SI 5((a) and (b)). It is seen that the fluorescence intensity inside the GUV lumen is almost the same until 55 s in Fig. SI 5(c) and 45 s in Fig. SI 5(e), then decays slowly with time. It takes about ~180 s to decrease from maximum intensity (i.e., 1.0) to ~ 0.1, which means that ~ 90% of the leakage occurred within about ~180 s.

We have mentioned in the main text, the time course of fluorescent intensity did not fit the single exponential decay function of Eq. 2 in the presence of membrane potential. Hence, we considered the logarithm of fluorescence intensity. The corresponding time-dependent logarithm of fluorescence intensity of Fig. SI 5(c) and SI 5(e) is shown in Fig. SI 5(d) and SI 5(f). To obtain the leakage constant, the experimental data is fitted with Eq. 2 where the solid red line represents the fitting curve. Hence, two rate constants k_{leak}^{i} and k_{leak}^{f} were obtained for the initial and final stage,s respectively. The values of k_{leak}^{i} and k_{leak}^{f} were obtained 11.68×10^{-3} s^{-1} and 5.62×10^{-3} s^{-1}, respectively for φ_m = −30 mV. Similarly, at φ_m = −60 mV, the values of k_{leak}^{i} and k_{leak}^{f} were obtained 16.54×10^{-3} s^{-1} and 4.42×10^{-3} s^{-1}, respectively. We have performed 3–5 independent experiments. At φ_m = −30 mV, the obtained average values of k_{leak}^{i} and k_{leak}^{f} were $(13.91 \pm 0.04)\times10^{-3}$ s^{-1} and $(4.80 \pm 0.04)\times10^{-3}$ s^{-1}, respectively, whereas, at φ_m = −60 mV the values of k_{leak}^{i} and k_{leak}^{f} were $(17.65 \pm 0.04)\times10^{-3}$ s^{-1} and $(3.46 \pm 0.06)\times10^{-3}$ s^{-1}, respectively. Thus, the leakage constant increases at the initial stage and decreases at the final stage as the φ_m increases.

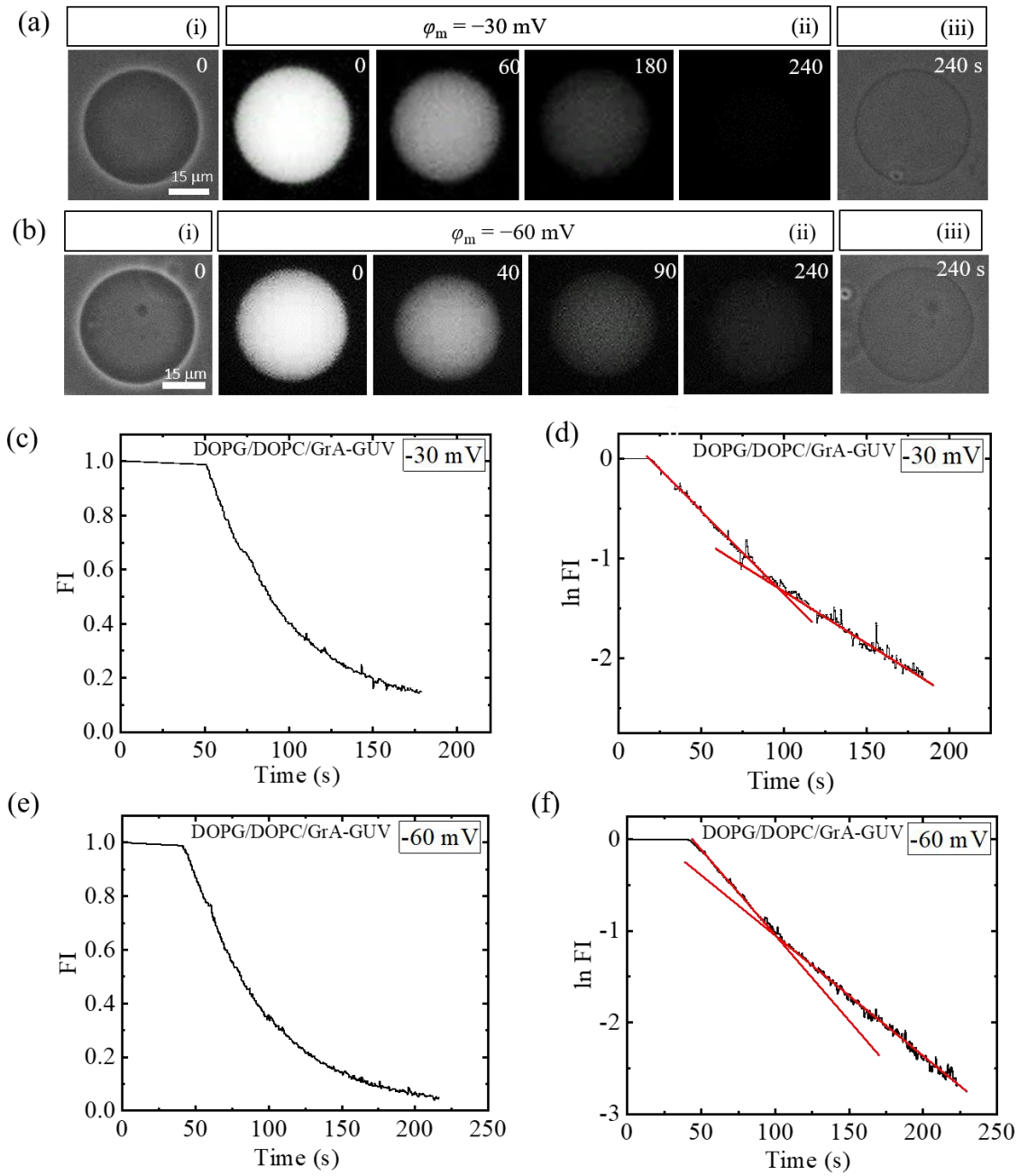

Fig. SI 5 Interaction of 2.0 µg/mL NPs with DOPG/DOPC/GrA (40/60/0.01)-GUVs in the presence of φ_m. Leakage of encapsulating calcein from the GUV at (a) φ_m = − 30 mV and (b) φ_m = − 60 mV. In (a) and (b), (i) and (iii) are the phase contrast images taken before and after the addition of NPs, respectively. (ii) The florescence images of the same GUV after addition of NPs. (c and e) The corresponding time course of the change in florescence intensity (FI) of the GUV as shown in Fig. (a) and (b). (d) and (f) represent the time course of logarithmic fluorescence intensity of (c) and (e), respectively. The solid red line is the fitting curve of Eq. 2.

SI 6. Leakage constant of encapsulating calcein of DOPG/DOPC/GrA (40/60/0.01)-GUVs

The results presented in sections 3.2 and 3.3 highlight the influence of membrane potential on the NPs-induced pore formation of DOPG/DOPC/GrA (40/60/0.01)-GUVs. Fig. SI 6(a) shows the time-dependent fluorescence intensity (FI) of a 'single GUV' at 0 mV, while Fig. SI 6(b) displays the corresponding FI at –90 mV. These figures provide a visual representation of the changes in FI over time under two different membrane potential conditions. To obtain the leakage constant (k_{leak}), the time-dependent FI was fitted with the following single exponential decay function (for zero membrane potential):

$$FI^{in}(t) = FI^{in}(t=0)\, exp\{-k_{leak}(t-t_0)\} \dots\dots\dots\dots\dots\dots\dots \text{(SI 1)}$$

where, $FI^{in}(t=0)$ is the initial intensity, $FI^{in}(t)$ is the intensity at any time, and t_0 is the starting time of the decay of FI (i.e., the starting time of poration). The time-dependent FI curves were fitted using Eq. SI 1, where the solid blue line represents the fitting curve in both figures. In Fig. 6(a), the fitting line overlaps with the experimental data. It means the leakage follows a single exponential decay function. In contrast, Fig. 6(b), the blue line doesn't overlap with the experimental data i.e., the leakage does not follow a single exponential decay function.

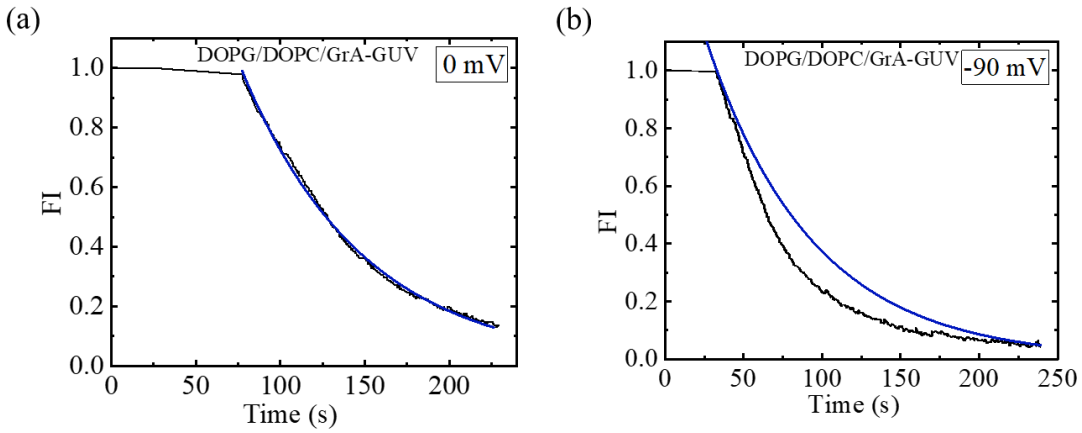

Fig. SI 6 The time dependent change in fluorescence intensity (FI) due to the interaction of 2.0 µg/mL NPs with DOPG/DOPC/GrA (40/60/0.01)-GUVs at (a) φ_m = 0 and (b) φ_m = − 90 mV. The solid blue line is the fitting curve of Eq. SI 1.

SI 7. Fitting procedure of NPs-induced encapsulating calcein leakage to obtain the value of leakage constant for initial and final stage

To conduct the fitting process, we utilized OriginLab software. Initially, we employed a first-order kinetic equation (Eq. 2) and observed that at φ_m = 0, the time-dependent FI followed a first-order kinetics. However, at higher φ_m, attempts to fit the data using second-order kinetic equation (Eq. SI 2), and the data did not conform to second-order kinetics. Subsequently, we fitted the time-dependent FI at higher φ_m using first-order kinetics, separately for two regimes, namely the initial and final stages. The second order kinetic equation is as follows:

$$\frac{1}{FI^{in}(t)} = \frac{1}{FI^{in}(t=0)} + k_{leak}(t - t_0) \quad \ldots\ldots\ldots\ldots\ldots\ldots\ldots (SI\ 2)$$

where, $FI^{in}(t=0)$ is the initial intensity, $FI^{in}(t)$ is the intensity at any time, and t_0 is the starting time of the decay of *FI* (i.e., the starting time of poration). In order to obtain the leakage constant at the initial stage, we plotted ln FI against time as depicted in Fig. SI 7(a). In our analysis, the initial stage was considered where the FI decreased from ~1.0 to 0.67 ± 0.05, while the final stage was considered where the FI decreased from 0.33 ± 0.05 to ~ 0. The selected portion was then fitted using Eq. 2. Similarly, for the final stage, we selected the last linear portion of the curve and performed fitting using Eq. 2, as illustrated in Fig. SI 7(b). This approach allowed us to estimate the leakage constants for the initial and final stages of the calcein leakage process.

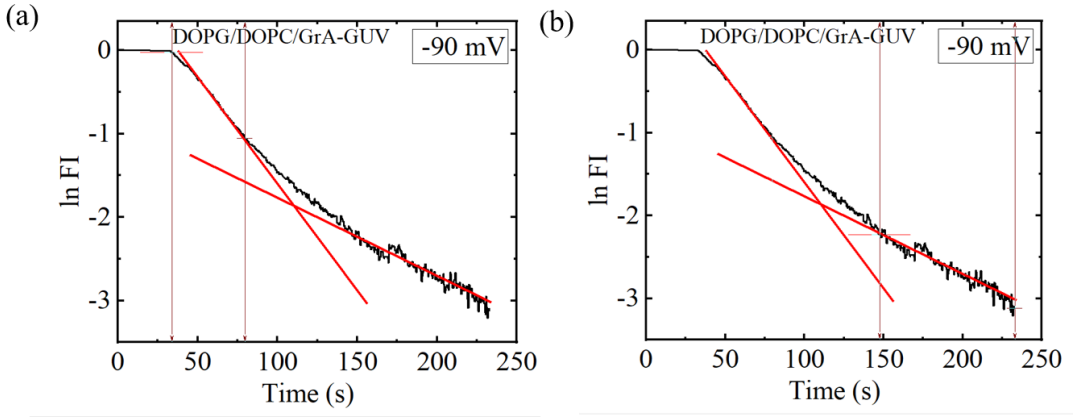

Fig. SI 7 The change in lnFI with time due to the interaction of 2.0 µg/mL NPs with DOPG/DOPC/GrA (40/60/0.01)-GUVs. The selection of data for the initial stage (a) and final stage (b) to getting the value of leakage constant.

SI 8. Fraction of deformation and fraction of poration of DOPG/DOPC (40/60)-GUVs under various concentrations of NPs at in absence of GrA and $\varphi_m = 0$

The time dependent fraction of deformation and fraction of poration of DOPG/DOPC (40/60)-GUVs due to the interaction of various concentrations of NPs at $\varphi_m = 0$ are presented in Fig. SI 8(a) and Fig. SI 8(b), respectively. The concertation dependent fraction of deformation and poration at 60 min is shows in Fig. SI 8(c). Both the fractions are increased with concentration but the value of deformation is higher than poration for each NPs concentration. From Fig. SI 8, it can be considered that the deformation and poration fractions appear to plateau to a constant average value after 40 mins.

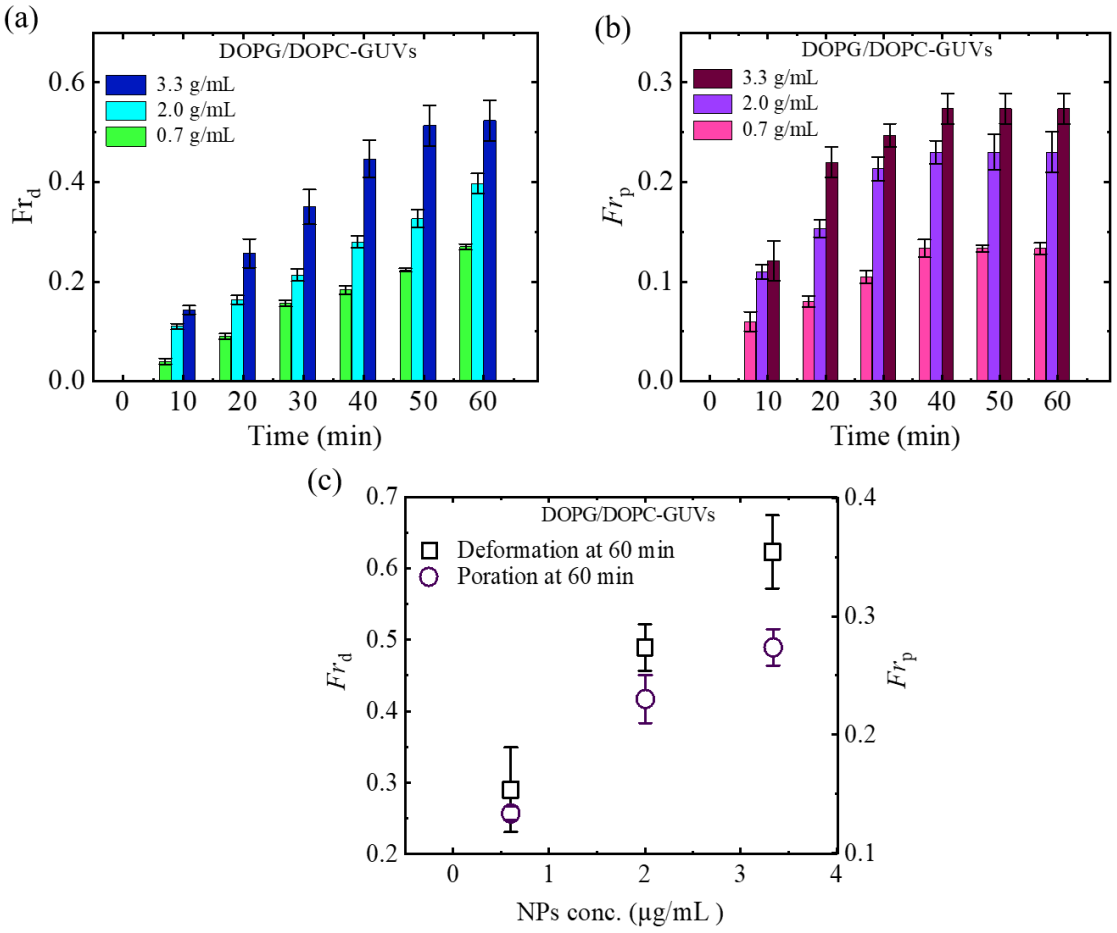

Fig. SI 8 The fraction of deformation and poration of DOPG/DOPC (40/60)-GUVs due to the interaction of various concentrations of NPs at $\varphi_m = 0$. (a) The time course of Fr_d at 0.7, 2.0 and 3.3 µg/mL NPs. (b) The time course of Fr_p at 0.7, 2.0 and 3.3 µg/mL NPs. (c) The NPs concentration dependent linear change of Fr_d and Fr_p.

SI 9. Adsorption of anionic magnetite NPs with lipid membrane in the presence of membrane potential

The adsorption of anionic magnetite NPs in the presence of membrane potential is discussed with an illustration (Fig. SI 9). The headgroup of DOPC forms a ($P^{-}-N^{+}$) dipole while forming membrane as shown in Fig. SI 9(a).[8] The head of DOPC maintains a 13° tilt angle on the membrane.[9] As the NPs are anionic, it binds with the positive pole (N^{+}) of the DOPC headgroup via Coulombic interaction, which induces a shift in the tilt angle. In contrast, Coulombic interaction of NPs with the negatively charged DOPG is also presented. We simplified the discussion by not considering the repulsive forces between the NPs and the dipoles of the membrane. However, it is important to note that these repulsive forces do exist and contribute to the overall membrane poration process. Hence, the interaction between NPs and N^{+} increases the dipole of the head of DOPC molecule depending on the adsorption site of NPs, which cause to decrease in the area of the outer monolayer.

The decrease in area of outer monolayer causes an inward lateral tension (σ) in the outer monolayer (Fig. SI 9(b)). Consequently, the same σ is induced in the inner monolayer at outward direction. This outward lateral tension may be responsible for the formation of a pre pore in the inner monolayer. On the other hand, line tension (Γ) is also present in the membrane, which tends to close the pre-pore formation.[10] Upon both actions (i.e., σ and Γ) in the membranes, prepore converts to transmembrane pore when the radius of the prepore exceeds a critical value. The encapsulating fluorescent calcein leaked out when transmembrane pores formed in the membranes. In addition, to this specific adsorption, the nonpolar regions of the lipid molecules can also interact with the NPs through van der Waals forces.[11,12] These forces arise from the attractive interactions between fluctuating dipoles in the lipid tails and the NPs surface.

In Fig. SI 9(b), we observe the adsorption of NPs onto the lipid membrane under a membrane potential of φ_m = –90 mV. As a consequence of this adsorption, a large-sized single pore is formed in the lipid bilayer, as depicted in Fig. SI 9(c). The creation of this pore leads to the expulsion of some of the previously adsorbed NPs from the membrane's surface. In this case, the K^{+} ions exchange between the inside and outside through the pore, resulting the decrease in the membrane potential. Moreover, Fig. SI 9(d) illustrates the progressive decrease in the pore's radius over time. This dynamic reduction in pore size directly impacts the leakage rate

of encapsulated calcein. The formation and dynamics of pore can have significant implications for the overall stability and functionality of the membrane, as well as for the cellular processes that involve ion transport and membrane permeability.

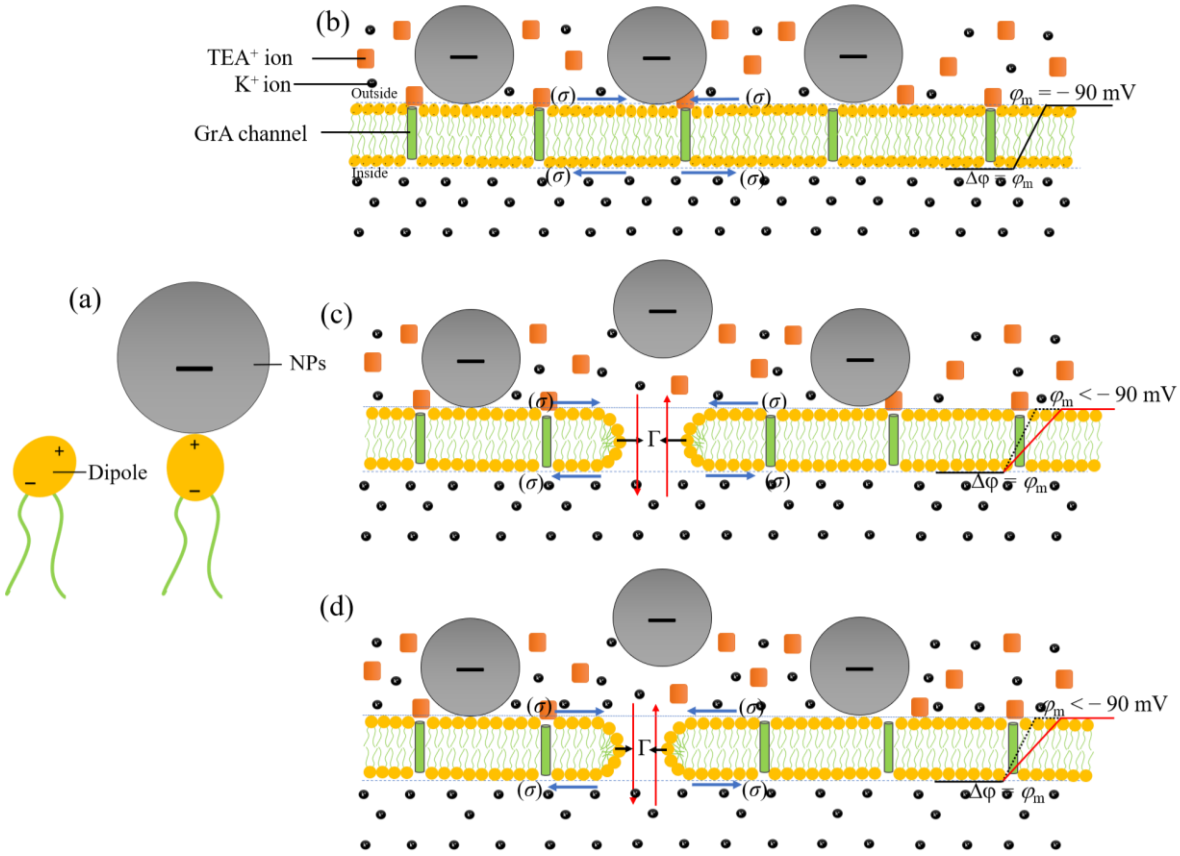

Fig. SI 9 Adsorption mechanism of anionic magnetite NPs in the presence of membrane potential. (a) Adsorption of NPs with DOPC lipid. (b) Adsorption of NPs with lipid membrane in the presence of φ_m = – 90 mV. (c) Formation of a large sized single pore in the bilayer and expulsion of NPs. Two parallel red arrows in vertical direction shows the exchange of K^+ through the pore between the inside and outside, resulting in decrease φ_m. (d) The pore radius decreases with time.

References

1 M. M. Zaman, M. A. S. Karal, M. N. I. Khan, A. R. M. Tareq, S. Ahammed, M. Akter, A. Hossain and A. K. M. A. Ullah, *ChemistrySelect*, 2019, **4**, 7824–7831.

2 M. A. S. Karal, S. Ahammed, V. Levadny, M. Belaya, M. K. Ahamed, M. Ahmed, Z. B. Mahbub and A. K. M. A. Ullah, *Chem. Phys. Lipids*, 2020, **230**, 104916.

3 Y. Tamba, H. Ariyama, V. Levadny and M. Yamazaki, *J. Phys. Chem. B*, 2010, **114**, 12018–12026.

4 M. M. R. Moghal, F. Hossain and M. Yamazaki, *Biophys. Rev.*, 2020, **12**, 339–348.

5 F. Hossain, H. Dohra and M. Yamazaki, *J. Bacteriol.*, 2021, **203**, 21–21.

6 F. Hossain, M. M. R. Moghal, M. Z. Islam, M. Moniruzzaman and M. Yamazaki, *J. Biol. Chem.*, 2019, **294**, 10449–10462.

7 O. S. Andersen, *Biophys. J.*, 1983, **41**, 135–146.

8 Z. E. Hughes, A. E. Mark and R. L. Mancera, *J. Phys. Chem. B*, 2012, **116**, 11911–11923.

9 H. P. Sang and S. J. Opella, *J. Mol. Biol.*, 2005, **350**, 310–318.

10 M. A. S. Karal, M. K. Ahamed, M. Ahmed and Z. B. Mahbub, *RSC Adv.*, 2021, **11**, 29598–29619.

11 J. Marra, *J. Coll. Interf. Sci.*, 1986, **109**, 11–20.

12 H. Nabika, A. Fukasawa and K. Murakoshi, *Langmuir*, 2006, **22**, 10927–10931.